

SUPER-RESOLUTION OF BVOC MAPS BY ADAPTING DEEP LEARNING METHODS

Antonio Giganti, Sara Mandelli, Paolo Bestagini, Marco Marcon, Stefano Tubaro

Dipartimento di Elettronica, Informazione e Bioingegneria - Politecnico di Milano - Milan, Italy

ABSTRACT

Biogenic Volatile Organic Compounds (BVOCs) play a critical role in biosphere-atmosphere interactions, being a key factor in the physical and chemical properties of the atmosphere and climate. Acquiring large and fine-grained BVOC emission maps is expensive and time-consuming, so most available BVOC data are obtained on a loose and sparse sampling grid or on small regions. However, high-resolution BVOC data are desirable in many applications, such as air quality, atmospheric chemistry, and climate monitoring. In this work, we investigate the possibility of enhancing BVOC acquisitions, further explaining the relationships between the environment and these compounds. We do so by comparing the performances of several state-of-the-art neural networks proposed for image Super-Resolution (SR), adapting them to overcome the challenges posed by the large dynamic range of the emission and reduce the impact of outliers in the prediction. Moreover, we also consider realistic scenarios, considering both temporal and geographical constraints. Finally, we present possible future developments regarding SR generalization, considering the scale-invariance property and super-resolving emissions from unseen compounds.

Index Terms— Biogenic Emissions, BVOC, Isoprene, Image Super-Resolution

1. INTRODUCTION

Terrestrial ecosystems generate many chemicals, including volatile and semi-volatile compounds released into the atmosphere. Some of them, such as Biogenic Volatile Organic Compounds (BVOCs), play critical roles in atmospheric chemistry [1], [2]. Their oxidation in the atmosphere affects tropospheric photochemistry and composition [3]. BVOC's oxidation products promote the formation of low-level ozone and secondary organic aerosols, thus significantly impacting air quality and the Earth's radiative budget [4], [5].

Quantitative estimations of BVOC emissions are required for numerical evaluations of past, current, and future air quality and climate conditions [1], [2], [6]. BVOC emissions are routinely included in coupled climate and chemistry models such as regional and global air quality and Earth system models [7]. Different ground-based measurement techniques can be applied to acquire BVOC emissions at diverse scales, from leaf to regional and global levels [5], [6]. However, available measurements are limited in space and time; therefore, they might not be fully suitable to perform reliable simulations of atmospheric, climate, and forecasting models.

We propose to overcome this issue by generating a denser spatial grid of BVOC emissions, starting from a coarser one. We formulate our goal as an image Super-Resolution (SR) task, a general problem of computationally enhancing the resolution of a digital image. Due to the ill-posed nature of this task, the goal of SR is to constrain

the problem of finding a unique mapping between a Low Resolution (LR) image and its High Resolution (HR) counterpart in such a way that the LR image is upscaled with high fidelity.

Several SR approaches have been proposed in the literature. Before the Deep Learning (DL) era, “classical” methods were based on different working principles (e.g., sparse neighbor embedding, edge sharpening, etc.). Starting with the seminal work of SR Convolutional Neural Network (SRCNN) [8], SR methods based on DL are nowadays widely exploited, proving superior to classical methods.

Applying image SR techniques to BVOC emissions is not straightforward. Indeed, many works focus on enhancing images that are evaluated by visual inspection (like photographs and biomedical data). However, BVOC data have a diverse nature, being physical measures linked to a meaningful measurement unit (e.g., we cannot observe negative emissions). Moreover, BVOC dynamic range is strongly different compared to classic 8-bit imagery. All these specific characteristics make the adaptation of standard SR methods a necessary operation for super-resolving BVOC emissions.

Dealing with data different from natural images is a well-known issue for researchers who apply SR algorithms to enhance the quality of satellite data [9]. For example, authors in [10] focused on improving the resolution of land surface temperature, while, recently, SR of sea surface temperature has been addressed in [11]–[13]. The improvement of trajectory calculations of wind fields has been tackled in [14], where authors implemented an attention mechanism to increase SR performances. Attention has also been used in [15] to face the SR of near-surface temperature. In [16], the authors exploited external factors and spatiotemporal dependencies of a pollution field to increase its resolution, and a similar problem was addressed in [17].

In this work, we tackle the problem of SR of BVOC emission maps. To the best of our knowledge, no prior studies are facing this task. The proposed investigations could provide dense data for the atmospheric chemical, climate, and air quality models. In addition, upsampling biogenic emission maps might be helpful for a variety of tasks, e.g., to capture small-scale processes, to improve characterization of the complex interaction between BVOCs and other chemical compounds, and to better quantify emissions induced from abiotic [18], [19] and ozone stress.

To solve our goal, we explore the potential of DL, investigating several state-of-the-art neural networks for SR. In particular, we study how to adapt these methods to the physical properties and the extremely wide dynamic range typical of BVOC emissions, investigating specific data transformations. The proposed method enables the synthesis of emission maps, making a significant step toward fulfilling the wishes of atmospheric chemical and climate modeling communities. Our main contributions are as follows:

- We explore seven DL-based SR algorithms to enhance the resolution of BVOC maps by a scale factor up to 4;
- We propose an appropriate data transformation to adapt SR methods to the BVOC domain by exploiting statistical information extracted from emissions;

This work was supported by the Italian Ministry of University and Research (MUR) and the European Union (EU) under the PON/REACT project.

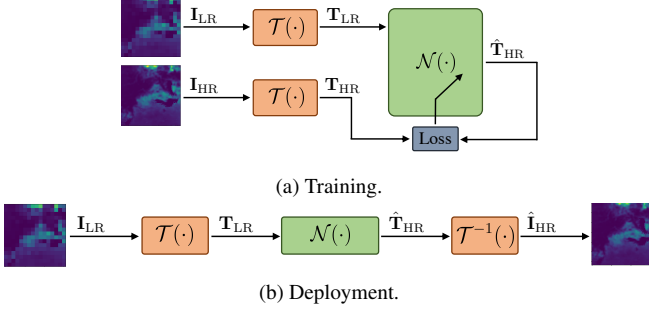


Fig. 1: The proposed method: (a) training and (b) deployment phase.

- We work with an extremely recent emission inventory, including highly-resolved biogenic global emissions [3];
- We investigate the generalization capabilities of the proposed methodology, involving spatial and temporal constraints, different spatial resolutions and compounds.

2. BVOC SUPER RESOLUTION

In this work, we consider the problem of recovering a High Resolution (HR) BVOC emission map \mathbf{I}_{HR} from a Low Resolution (LR) emission map \mathbf{I}_{LR} , which can be seen as an image Super-Resolution (SR) task. Fig. 1 shows a sketch of the proposed methodology. We estimate a super-resolved emission $\hat{\mathbf{I}}_{\text{HR}}$ starting from the LR emission \mathbf{I}_{LR} as

$$\hat{\mathbf{I}}_{\text{HR}} = \mathcal{T}^{-1}(\mathcal{N}(\mathcal{T}(\mathbf{I}_{\text{LR}}))), \quad (1)$$

where $\mathcal{T}(\cdot)$ is a transformation applied to the LR emission, $\mathcal{N}(\cdot)$ is the operator applied by a neural network, and $\mathcal{T}^{-1}(\cdot)$ is the inverse transformation of $\mathcal{T}(\cdot)$. We model \mathbf{I}_{LR} as a matrix with size $M \times N$, while \mathbf{I}_{HR} and its estimation $\hat{\mathbf{I}}_{\text{HR}}$ have size $\alpha M \times \alpha N$, with $\alpha > 1$ indicating the SR factor (i.e., how much we increase the resolution).

The network training phase involves $(\mathbf{I}_{\text{LR}}, \mathbf{I}_{\text{HR}})$ emission pairs as input (see Fig. 1a). We consider the Mean Squared Error (MSE) between the transformed emissions as a loss function. At testing stage (see Fig. 1b), given an \mathbf{I}_{LR} emission to be super-resolved, we estimate $\hat{\mathbf{T}}_{\text{HR}}$ from the network. Then, we return to the original emission's range by applying the inverse data transformation $\mathcal{T}^{-1}(\cdot)$, obtaining the super-resolved emission $\hat{\mathbf{I}}_{\text{HR}}$.

2.1. Data Transformation

BVOC emissions are spatially sparse, reporting extremely small values and a wide dynamic range (from 10^{-30} to 10^{-9} [kg/m²s] [3]). Transforming this dynamic into more feasible values is crucial for numerical stability when training the network. To obtain emission maps with a dynamic range in $[0, 1]$, we investigate two data transformation strategies, obtaining $\mathbf{T}_{\text{LR}} = \mathcal{T}(\mathbf{I}_{\text{LR}})$ and $\mathbf{T}_{\text{HR}} = \mathcal{T}(\mathbf{I}_{\text{HR}})$, respectively:

- \mathcal{T}_{S} — *Emission Scaling*: the transformed emissions are obtained by dividing \mathbf{I}_{LR} and \mathbf{I}_{HR} by their maximum, i.e.,

$$\mathbf{T}_{\text{LR}} = \mathbf{I}_{\text{LR}}/\mathbf{I}_{\text{LR,max}}, \quad \mathbf{T}_{\text{HR}} = \mathbf{I}_{\text{HR}}/\mathbf{I}_{\text{HR,max}}; \quad (2)$$

- \mathcal{T}_{E} — *Emission Equalization*: \mathbf{T}_{LR} and \mathbf{T}_{HR} are obtained by transforming \mathbf{I}_{LR} and \mathbf{I}_{HR} values to follow a uniform distribution between 0 and 1 [20]. In particular, we propose to learn the data transformation at training stage from HR emission maps. In a nutshell, we extract information on the Cumulative Distribution Function (CDF) of training data by subdividing them into different

quantiles, associating a specific CDF value with each training data quantile. Then, we apply this CDF to all the emission maps for transforming them. To be more precise, for every possible emission value K of HR maps belonging to the training set, we can define the associated CDF value as

$$F(K) = \sum_{k=K_{\min}}^K p_k, \quad (3)$$

where K_{\min} is the lowest observed HR emission value during training and p_k is the probability that training HR maps assume the value k . We compute the transformed emission maps \mathbf{T}_{HR} and \mathbf{T}_{LR} as

$$[\mathbf{T}_{\text{HR}}]_{i,j} = F([\mathbf{I}_{\text{HR}}]_{i,j}), \quad [\mathbf{T}_{\text{LR}}]_{i,j} = F([\mathbf{I}_{\text{LR}}]_{i,j}), \quad (4)$$

where i, j are the row and column coordinates of the emission values in each map. Notice that, since $F(K) \in [0, 1] \forall K$, the transformed emission maps also cover this value range.

Most of the past works in SR for 2D data that involve physical quantities simply scale the input according to the \mathcal{T}_{S} approach [10], [12], [15], discarding the intrinsic correlation of adjacent values. On the contrary, it has been proven that transforming data using statistical information extracted from quantiles of the input data distribution (i.e., \mathcal{T}_{E} transformation) is less influenced by outliers than \mathcal{T}_{S} preprocessing [20], [21] and can lead to better predictions [22]. This property is beneficial for BVOC emissions since there can be many outliers due to the large spatial diversity of the environmental factors driving the emission process, such as meteorology, type of vegetation, seasonal cycle, and atmospheric composition [3].

Another difference between the two transformations is related to retrieving information on the maximum peak emission. Indeed, due to the inherent low resolution of LR maps, it is common to miss out the maximum emission value of HR maps in their related LR version. In other words, it may happen very often that $\mathbf{I}_{\text{LR,max}} < \mathbf{I}_{\text{HR,max}}$, for each $(\mathbf{I}_{\text{LR}}, \mathbf{I}_{\text{HR}})$ pair. If this happens, \mathcal{T}_{S} provides a processed version of \mathbf{I}_{LR} not consistent with the data distribution in \mathbf{I}_{HR} . On the contrary, \mathcal{T}_{E} performs a non-linear transformation based on *a priori* information derived from statistical analysis of the HR data. This is not sensitive to single outliers or local maxima in the data, making the distribution of \mathbf{I}_{LR} and \mathbf{I}_{HR} transformed data compatible.

2.2. SR Networks

We compare seven different state-of-the-art neural networks for image SR, investigating the adoption of different configurations and learning paradigms. The investigated networks are the following:

- SRCNN [8], which is a pioneer work based on Convolutional Neural Networks (CNNs);
- Super-Resolution Generative Adversarial Network (SRGAN) [23], where the authors define a novel perceptual loss based on feature maps of the Visual Geometry Group (VGG) network;
- Residual Channel Attention Network (RCAN) [24], which is an attention-based framework. The recursive residual design allows multiple pathways for information flow from initial to final layers, and selective attention allows focusing on specific feature maps that are more important for the end task;
- Enhanced SRGAN (ESRGAN) [25], which is an improved version of SRGAN [23], including a different architecture for both the generator and the discriminator;

- Residual-in-Residual Dense Block Network (RRDBNet) [25], combining multi-level residual networks and dense connections;
- Second-order Channel Attention Network (SANSISR) [26], where Second-order Attention Network (SAN) is proposed for more powerful feature correlation learning, using second-order feature statistics. The authors propose an additional block to capture long-distance spatial information and to exploit LR information, easing the training and bypassing low-frequency characteristics;
- Modified SRResNet (MSRResNet) [27], which is a modified version of the original Super-Resolution ResNet (SRResNet) [23], exploiting the benefits of the residual learning framework.

3. EXPERIMENTAL SETUP

3.1. Dataset

Inventories of real measurements of BVOC emissions are scarce and limited in time and space. However, the knowledge obtained from observations on the emission processes gives the possibility to simulate them for a specific temporal and spatial domain based on defined input parameters. We use the most recent global coverage biogenic emission inventory calculated by an emission model and presented in [3]. The inventory includes emissions from several biogenic compounds, covering the entire Earth surface from 2000 to 2019, with a $0.25^\circ \times 0.25^\circ$ spatial resolution ($\approx 28\text{km} \times 28\text{km}$ of the planet surface for each cell in continental regions). As far as we know, this is the most up-to-date global coverage biogenic emission inventory with the highest spatial resolution available in the literature. Emissions are reported as hour profiles and are averaged monthly.

Among the different biogenic compounds in the inventory, we select isoprene since it is by far the most important in terms of both global emission and atmospheric impact [3], [5], with an annual emission of about half of the total BVOCs emissions [18].

Each emission map has a grid of 1440×720 cells. We slice them to obtain smaller non-overlapped patches of size 64×64 cells. This makes the training more computationally manageable and allows us to assume that there are not many radial distortions due to the Earth curvature in the area. Since these maps are spatially sparse, a considerable amount contains zero emissions. Thus, we discard the patches with non-zero emissions below 5%, avoiding unnecessary computation on zero-emission areas. We end up with 81957 different HR patches \mathbf{I}_{HR} that can be considered as ground truth. We generate the associated LR patches by performing bicubic down-sampling, obtaining the \mathbf{I}_{LR} emission maps of 16×16 cells. The $(\mathbf{I}_{\text{LR}}, \mathbf{I}_{\text{HR}})$ pairs constitute our final dataset $\mathcal{D} = \{\mathbf{I}_{\text{HR}_i}, \mathbf{I}_{\text{LR}_i}\}$, for $i = 1, \dots, 81957$. We aim at super-resolving LR emission maps, which have a $1^\circ \times 1^\circ$ spatial resolution, into HR emission maps with $0.25^\circ \times 0.25^\circ$ resolution, thus with scale factor $\alpha = 4$.

3.2. Training Setting

As reported in Sec. 2.1, \mathcal{T}_E transformation requires the estimation of the CDF of HR training data for mapping the emission probability distribution to the uniform one [20]. We estimate this CDF by exploiting all HR training data, dividing their dynamics into 1000 quantiles. Then, we preprocess \mathbf{I}_{HR} and \mathbf{I}_{LR} emissions with this estimated transformation. We keep this transformation fixed for what concerns further network training and deployment stages.

To train the networks, we divide our dataset into train, validation, and test sets with 70/20/10 percentage amount, respectively. We combine the ADAM optimizer with the Cosine Annealing (with restarts) learning rate scheduler, which enables to obtain faster computations and better results [28]. We use $50k$ iterations with restarts

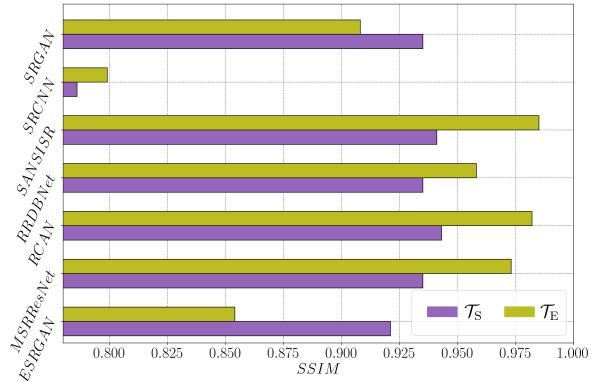


Fig. 2: Average SSIM achieved by the different networks, for \mathcal{T}_S and \mathcal{T}_E data transformations.

equal to 1 at iteration $10k$, $20k$, and $40k$. The initial learning rate is 10^{-4} , with a minimum value of 10^{-7} .

4. RESULTS

4.1. Metrics

To evaluate the performance of our method, we employ the Structural Similarity Index Measure (SSIM), a well-known metric for quantifying the resemblance between two images. We also adopt the Normalized Mean Squared Error (NMSE), defined as the MSE between \mathbf{I}_{HR} and $\hat{\mathbf{I}}_{\text{HR}}$, normalized by the average of \mathbf{I}_{HR} ². A good result is the one with high SSIM and/or low NMSE.

4.2. Preliminary Studies

We compare the networks' performance for a single scale factor $\alpha = 4$ and two different data transformations (i.e., \mathcal{T}_S or \mathcal{T}_E). Fig. 2 summarizes the results in terms of SSIM. We can notice a reasonably high quality on all the architectures except for the SRCNN, with a significant boost on attention-based networks (i.e., SANSISR and RCAN). It is worth noticing that \mathcal{T}_E preprocessing almost always reports better reconstruction results than \mathcal{T}_S strategy. Given these reasons, we adopt \mathcal{T}_E transformation in all the remaining experiments. In Fig. 3, we report an example of super-resolved emission maps from the best-performing networks.

4.3. Solving Realistic Scenarios

In this section, we investigate the performance of our method over more realistic and challenging scenarios. In particular, we aim to perform SR of emission profiles in a different time range and geographical areas than those used in the training phase. In a real-world context, the possibility to train with past data and test on future data would be a highly desirable feature. Moreover, the availability of training data inherent to the same geographic area may be infeasible. As mentioned previously, measurements of biogenic emissions are often limited to restricted geographical areas. To address these scenarios, from the main dataset \mathcal{D} we build two subsets:

- \mathcal{D}_T — *Time*: we consider patches from years 2000-2014 for training, from years 2014-2018 for validation and years 2018-2019 for testing. This prevents the network from learning inter-annual biases and enables to investigate the temporal dependence.
- \mathcal{D}_{TA} — *Time & Area*: a split version of \mathcal{D}_T dataset that considers a portion of the spatial coverage for training and the remaining part for testing. This enables to investigate spatial dependence.

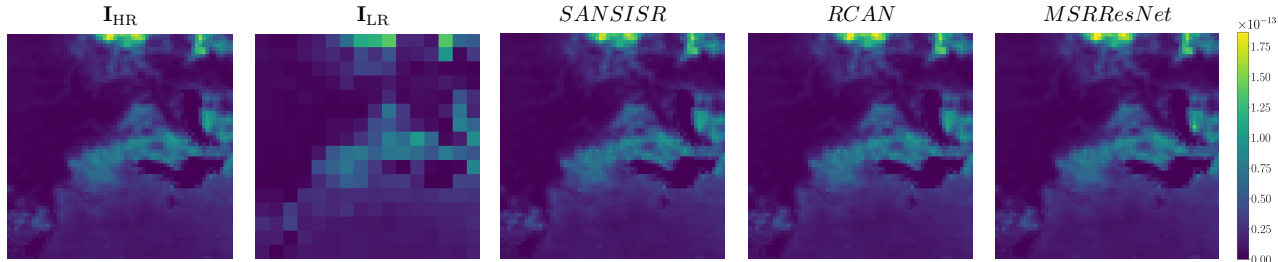


Fig. 3: Image SR examples of a generic BVOC emission map from different algorithms. From left to right, the ground truth HR image, the input LR image, and three super-resolved results.

Table 1: Performance results over the datasets \mathcal{D} , \mathcal{D}_T and \mathcal{D}_{TA} .

Dataset	SANSISR	RCAN	MSRResNet
	SSIM / NMSE [dB]	SSIM / NMSE [dB]	SSIM / NMSE [dB]
\mathcal{D}	0.984 / -19.35	0.982 / -19.26	0.970 / -17.27
\mathcal{D}_T	0.986 / -21.50	0.985 / -20.44	0.973 / -17.66
\mathcal{D}_{TA}	0.769 / -7.31	0.774 / -7.32	0.788 / -7.26

We compare the performances of our method over \mathcal{D}_T and \mathcal{D}_{TA} with those achieved on the initial dataset \mathcal{D} . Notice that \mathcal{D}_{TA} contains the smallest amount of emission pairs due to temporal and geographical constraints. To fairly compare the three scenarios, we randomly sample the bigger datasets \mathcal{D}_T and \mathcal{D} to have the same cardinality as \mathcal{D}_{TA} . For simplicity, we compare only the three best-performing networks namely, SANSISR, RCAN, and MSRResNet.

Results are shown in Table 1. The three networks perform very similarly, with SANSISR achieving the best results in most cases. It is worth noticing that we can super-resolve unseen emissions from different years (i.e., \mathcal{D}_T results). On the contrary, the performance drops drastically when dealing with geographical areas unseen in the training phase (i.e., \mathcal{D}_{TA} results). This worse result occurs because of the close link between biogenic emissions and land morphology and the vegetation type of the area used in training.

4.4. Towards Generalization in Emissions Super-Resolution

In this section, we address two relevant problems related to the application of SR methods on BVOC emission maps. In particular, we investigate the scale-invariance and the estimation of different compounds. We only show results related to SANSISR architecture, being it the best-performing one among the employed networks.

Scale-invariance. This property concerns the ability to generalize SR to data with a spatial resolution not present in training. This could be a useful feature of SR algorithms embedded in the climate modeling frameworks. For instance, if we train the network to pass from $1.00^\circ \times 1.00^\circ$ to $0.25^\circ \times 0.25^\circ$ spatial resolution (i.e., with a $\alpha = 4$ scale factor), we aim at testing the network capabilities in super-resolving emissions from $2.00^\circ \times 2.00^\circ$ to $0.50^\circ \times 0.50^\circ$ (i.e., the scale factor remains the same but the spatial resolution changes).

We investigate the scale-invariance in super-resolving emissions at two scale factors, i.e., $\alpha = 2$ and $\alpha = 4$. Table 2(a) reports the experimental results. As expected, we achieved excellent performance testing data with the exact spatial resolution used in training. Whereas, for both $\alpha = 2$ and $\alpha = 4$ scale factors, testing over unseen resolutions leads to significant drops in performance. This indicates that scale-invariance hypotheses are not fully satisfied.

Estimation of different compounds. We investigate the SR of emission maps utilizing compounds different than those adopted in training. As the scale-invariance, this property could be a desirable

Table 2: Results for the scale-invariance (a) and for the estimation of different compounds (b). The configuration used during the training phase is reported in bold.

(a)			(b)	
Scale Factor	Spatial Resolution	SSIM / NMSE [dB]	Biogenic Species	SSIM / NMSE [dB]
	$0.50^\circ \rightarrow 0.25^\circ$	0.993 / -25.58	\mathcal{D}	0.985 / -20.87
$\alpha = 2$	$1.00^\circ \rightarrow 0.50^\circ$	0.834 / -8.41	\mathcal{D}_{mon}	0.875 / -15.76
	$2.00^\circ \rightarrow 1.00^\circ$	0.659 / -5.24	\mathcal{D}_{met}	0.752 / -13.30
$\alpha = 4$	$1.00^\circ \rightarrow 0.25^\circ$	0.985 / -20.86	\mathcal{D}_{ses}	0.905 / -16.03
	$2.00^\circ \rightarrow 0.50^\circ$	0.603 / -4.84		

feature in atmospheric modeling frameworks for enhancing the resolution of a generic chemical compound.

We build three datasets similar to \mathcal{D} but containing emissions of diverse compounds. We select monoterpenes (\mathcal{D}_{mon}), methanol (\mathcal{D}_{met}), and sesquiterpenes (\mathcal{D}_{ses}), since these are the most responsible compounds for the majority of the global BVOC emission [3]. We train our method over the reference dataset \mathcal{D} and test on the three datasets. Results are depicted in Table 2(b). Given the similarity of their chemical structure with that of isoprene, it is worth noticing that terpenoids like monoterpenes (i.e., \mathcal{D}_{mon}) and sesquiterpenes (i.e., \mathcal{D}_{ses}) could be used as input to our algorithm, with results that are still acceptable if we consider the benefits that SR emission maps could give to air quality and climate models.

5. CONCLUSIONS

This work focused on enhancing the spatial resolution of BVOC emission maps using DL techniques, proposing a suitable data transformation that drastically reduces the impact of outliers and improve the accuracy and reliability of our models. Super-resolution of BVOC emission maps is critical since global inventories of BVOC measurements are currently unavailable to the modeling communities, and processing existing emissions appears to be the only way to produce maps with high spatial resolution.

The overall high performance of the proposed method shows that we effectively generalize to unseen data, achieving accurate estimations of potential future BVOC emissions. We also indicate possible avenues towards improvements in the algorithms' generalization, investigating scale-invariance, and testing different compounds. In the future, we will extend our work through the use of Physics-Informed Neural Networks (PINN), considering both data and the physics behind the process. Super-resolved BVOC emissions could represent an invaluable source for air quality and climate products, allowing us to explain better how these compounds affect humans and global climate change.

6. REFERENCES

- [1] M. Cai, C. An, and C. Guy, “A scientometric analysis and review of biogenic volatile organic compound emissions: Research hotspots, new frontiers, and environmental implications,” *Renewable and Sustainable Energy Reviews*, vol. 149, pp. 1–15, 2021.
- [2] A. B. Guenther, X. Jiang, C. L. Heald, *et al.*, “The Model of Emissions of Gases and Aerosols from Nature version 2.1 (MEGAN2.1): An extended and updated framework for modeling biogenic emissions,” *Geoscientific Model Development*, vol. 5, pp. 1471–1492, 2012.
- [3] K. Sindelarova, J. Markova, D. Simpson, *et al.*, “High-resolution biogenic global emission inventory for the time period 2000–2019 for air quality modelling,” *Earth System Science Data*, vol. 14, pp. 251–270, 2022.
- [4] P. Ciccioli, C. Silibello, S. Finardi, *et al.*, “The potential impact of biogenic volatile organic compounds (BVOCs) from terrestrial vegetation on a mediterranean area using two different emission models,” *Agricultural and Forest Meteorology*, vol. 328, p. 109255, 2023.
- [5] B. Opacka, J.-F. Müller, T. Stavrakou, *et al.*, “Global and regional impacts of land cover changes on isoprene emissions derived from spaceborne data and the MEGAN model,” *Atmospheric Chemistry and Physics*, vol. 21, no. 11, pp. 8413–8436, 2021.
- [6] C. N. Hewitt, B. Langford, M. Possell, *et al.*, “Quantification of VOC emission rates from the biosphere,” *TrAC Trends in Analytical Chemistry*, vol. 30, pp. 937–944, 2011.
- [7] K. W. Appel, J. O. Bash, K. M. Fahey, *et al.*, “The community multiscale air quality (CMAQ) model versions 5.3 and 5.3.1: System updates and evaluation,” *Geoscientific Model Development*, vol. 14, no. 5, pp. 2867–2897, 2021.
- [8] C. Dong, C. C. Loy, K. He, and X. Tang, “Learning a Deep Convolutional Network for Image Super-Resolution,” in *European Conference on Computer Vision (ECCV)*, 2014.
- [9] F. Salvetti, V. Mazzia, A. Khaliq, and M. Chiaberge, “Multi-Image Super Resolution of Remotely Sensed Images Using Residual Attention Deep Neural Networks,” *Remote Sensing*, vol. 12, p. 2207, 2020.
- [10] B. M. Nguyen, G. Tian, M.-T. Vo, *et al.*, “Convolutional neural network modelling for MODIS land surface temperature super-resolution,” in *European Signal Processing Conference (EUSIPCO)*, 2022, pp. 1806–1810.
- [11] B. Ping, F. Su, X. Han, and Y. Meng, “Applications of deep learning-based super-resolution for sea surface temperature reconstruction,” *IEEE Journal of Selected Topics in Applied Earth Observations and Remote Sensing*, vol. 14, pp. 887–896, 2021.
- [12] T. Izumi, M. Amagasaki, K. Ishida, and M. Kiyama, “Super-resolution of sea surface temperature with CNN and GAN-based methods,” *Journal of Water and Climate Change*, vol. 13, pp. 1673–1683, 2022.
- [13] D. T. Lloyd, A. Abela, R. A. Farrugia, *et al.*, “Optically Enhanced Super-Resolution of Sea Surface Temperature Using Deep Learning,” *IEEE Transactions on Geoscience and Remote Sensing*, vol. 60, pp. 1–14, 2022.
- [14] R. Brecht, L. Bakels, A. Bihlo, and A. Stohl, “Improving trajectory calculations by FLEXPART 10.4+ using deep learning inspired single image superresolution,” *EGUsphere*, vol. 2022, pp. 1–17, 2022.
- [15] Y. Yasuda, R. Onishi, Y. Hirokawa, *et al.*, “Super-resolution of near-surface temperature utilizing physical quantities for real-time prediction of urban micrometeorology,” *Building and Environment*, vol. 209, 2022.
- [16] N. Liu, R. Ma, Y. Wang, and L. Zhang, “Inferring fine-grained air pollution map via a spatiotemporal super-resolution scheme,” in *ACM UbiComp/ISWC Adjunct*, 2019, pp. 498–504.
- [17] B. Bessagnet, M. Beauchamp, L. Menut, *et al.*, “Deep learning techniques applied to super-resolution chemistry transport modeling for operational uses,” *Environmental Research Communications*, vol. 3, no. 8, p. 085001, 2021.
- [18] A. Tani and T. Mochizuki, “Review: Exchanges of volatile organic compounds between terrestrial ecosystems and the atmosphere,” *Journal of Agricultural Meteorology*, vol. 77, no. 1, pp. 66–80, 2021.
- [19] J. Feldner, M. O. P. Ramacher, M. Karl, *et al.*, “Analysis of the effect of abiotic stressors on BVOC emissions from urban green infrastructure in northern Germany,” *Environmental Science: Atmospheres*, vol. 2, no. 5, pp. 1132–1151, 2022.
- [20] F. Pedregosa, G. Varoquaux, A. Gramfort, *et al.*, “Scikit-learn: Machine learning in Python,” *Journal of Machine Learning Research*, vol. 12, pp. 2825–2830, 2011.
- [21] K. Bogner, F. Pappenberger, and H. L. Cloke, “Technical note: The normal quantile transformation and its application in a flood forecasting system,” *Hydrology and Earth System Sciences*, vol. 16, no. 4, pp. 1085–1094, 2012.
- [22] R. A. Peterson and J. E. Cavanaugh, “Ordered quantile normalization: A semiparametric transformation built for the cross-validation era,” *Journal of Applied Statistics*, vol. 47, no. 13–15, pp. 2312–2327, 2020.
- [23] C. Ledig, L. Theis, F. Huszar, *et al.*, “Photo-Realistic Single Image Super-Resolution Using a Generative Adversarial Network,” in *IEEE Conference on Computer Vision and Pattern Recognition (CVPR)*, 2017.
- [24] Y. Zhang, K. Li, K. Li, *et al.*, “Image Super-Resolution Using Very Deep Residual Channel Attention Networks,” in *European Conference on Computer Vision (ECCV)*, 2018.
- [25] X. Wang, K. Yu, S. Wu, *et al.*, “ESRGAN: Enhanced Super-Resolution Generative Adversarial Networks,” in *European Conference on Computer Vision (ECCV)*, 2019.
- [26] T. Dai, J. Cai, Y. Zhang, *et al.*, “Second-Order Attention Network for Single Image Super-Resolution,” in *IEEE Conference on Computer Vision and Pattern Recognition (CVPR)*, 2019.
- [27] K. Zhang, S. Gu, R. Timofte, *et al.*, “AIM 2019 challenge on constrained super-resolution: Methods and results,” in *IEEE/CVF International Conference on Computer Vision Workshop (ICCVW)*, 2019, pp. 3565–3574.
- [28] I. Loshchilov and F. Hutter, “Decoupled Weight Decay Regularization,” in *International Conference on Learning Representations (ICLR)*, 2019.